



CHORUS

This is the accepted manuscript made available via CHORUS. The article has been published as:

## Single qubit operations using microwave hyperbolic secant pulses

H. S. Ku, J. L. Long, X. Wu, M. Bal, R. E. Lake, Edwin Barnes, Sophia E. Economou, and D. P. Pappas

Phys. Rev. A **96**, 042339 — Published 30 October 2017

DOI: [10.1103/PhysRevA.96.042339](https://doi.org/10.1103/PhysRevA.96.042339)

# Single qubit operations using microwave hyperbolic secant pulses

H. S. Ku,<sup>1,\*</sup> J. L. Long,<sup>1,2</sup> X. Wu,<sup>1</sup> M. Bal,<sup>1</sup> R. E. Lake,<sup>1</sup> Edwin Barnes,<sup>3</sup> Sophia E. Economou,<sup>3</sup> and D. P. Pappas<sup>1</sup>

<sup>1</sup>*National Institute of Standards and Technology, Boulder, Colorado 80305, USA*

<sup>2</sup>*Department of Physics, University of Colorado, Boulder, Colorado 80309, USA*

<sup>3</sup>*Department of Physics, Virginia Tech, Blacksburg, Virginia 24061, USA*

(Dated: September 29, 2017)

It has been known since the early days of quantum mechanics that hyperbolic secant pulses possess the unique property that they can perform full-cycles Rabi oscillation on two-level quantum systems independently of the pulse detuning. More recently, it was realized that they induce detuning-controlled phases without changing state populations. Here, we experimentally demonstrate the properties of hyperbolic secant pulses on superconducting transmon qubits and contrast them with the more commonly used Gaussian and square waves. We further show that these properties can be exploited to implement phase gates, nominally without exiting the computational subspace. This enables us to demonstrate the first microwave-driven  $Z$ -rotation with a single control parameter, the detuning.

PACS numbers: 03.67.Lx

Controlled rotations of two-level systems were among the first examples of time-dependent quantum phenomena ever studied and continue to be a very active area of research owing to the central role they play in numerous quantum-based technologies currently being pursued [1–4]. Early investigations of two-level quantum dynamics were conducted using a double Stern-Gerlach experiment in which spins traverse a region of rotating magnetic field [5]. In the rotating frame, this problem can be mapped onto the familiar Rabi oscillations of atoms in a field [6], where the time-dependent drive amplitude,  $\Omega(t)$ , and the detuning,  $\Delta$ , from the two-level energy splitting correspond to the magnetic field strength and precession rate of the spins in the field, respectively. It was recognized early on by Rosen and Zener [7] that there is an exact solution to this problem, with  $\Omega(t) = \Omega_0 \operatorname{sech}(\rho t)$ . More importantly, for specific values of  $\Omega_0$ , a spin in an arbitrary superposition of  $|0\rangle$  and  $|1\rangle$  will always return back to that same initial state, i.e. cyclic evolutions, *independently* of the value of the detuning. This surprising result has been leveraged extensively in fields such as spatial solitons, quantum optics and self-induced transparency [8–11]. The cyclic evolution is accompanied by the acquisition of opposite phases by states  $|0\rangle$  and  $|1\rangle$ , which has been suggested [12–16] as a means to implement phase gates or multi-qubit entangling gates in various qubit systems through the use of states outside the computational subspace.

Single-qubit gates are required for quantum computing and simulations. In the case of rotations about an axis in the  $XY$  plane, the control design is rather straightforward: a resonant pulse of any shape will implement such a rotation, with the pulse area (the time integral of the pulse envelope) determining the angle of rotation. The theoretical simplicity of this concept has made qubit rotations about  $XY$  axes routine in many labs [17–20].

On the other hand,  $Z$ -rotations have been implemented to date via tuning [21], combining rotations about  $X$  and  $Y$  using multiple pulses, or just by keeping an accounting of all phases on the system [22]. In general, these methods can result in increased decoherence in systems of multiple qubits, as it takes the parameters away from the high coherence regime. The other alternatives can result in increased overhead in pulse time or accounting. There is thus a need for a gate that achieves a rotation around the  $Z$ -axis using a single pulse to simplify and reduce overheads.

One of the difficulties in implementing  $Z$ -rotations (i.e. phase gates) is that, unlike in the case of rotations about axes in the  $XY$  plane, there is no generic analytical solution for the evolution operator corresponding to a  $Z$ -rotation. One general requirement for phase gates is that the qubit undergoes a full Rabi cycle, with all populations restored to their initial values. This can be achieved with resonant  $2\pi$  pulses, however such pulses induce the same phase factor (equal to -1) to both the  $|0\rangle$  and the  $|1\rangle$  state, resulting in a trivial qubit operation that does not change the phase.

In the current work, we overcome this challenge and develop the first implementation of a microwave-mediated  $Z$ -rotation,  $Z_{\operatorname{sech}}(\Delta)$ . By using a sech-function microwave pulse, we are able to achieve a phase gate in qubits using only a single parameter, the detuning  $\Delta$ , and nominally driving the lower two levels of a transmon qubit. After fixing the peak strength of the pulse to satisfy the full Rabi cycle condition, the detuning is used to adjust the angle of rotation. Here we demonstrate the general result that this property is unique to the sech pulse, in contrast with other pulse shapes such as square and Gaussian, and demonstrate that sech pulses can be used to generate microwave-based phase gates that are intrinsically high-fidelity,  $F > 99\%$ .

To demonstrate a  $Z$ -rotation with superconducting qubits, we use a microwave pulse with a sech-envelope to rotate between the lowest two energy levels of a trans-

---

\* Hsiang-Sheng.Ku@nist.gov

mon. We consider a two-level system coupled by an external drive field, where the time-dependent Rabi frequency  $\Omega(t)$  of the drive pulse is defined as [12]

$$\Omega(t) = \Omega_0 \operatorname{sech}(\rho t) \cos(\omega_D t), \quad (1)$$

where  $\Omega_0$  is the peak drive amplitude,  $\rho$  is the pulse bandwidth, and  $\omega_D$  is the drive frequency. After the rotating wave approximation, the full Rabi cycle condition is satisfied by choosing

$$\Omega_0/\rho = n, \quad (2)$$

where  $n$  is an integer [7, 10]. The salient feature is that this cyclic evolution condition is independent of  $\omega_D$ . This enables us to devise a single-control microwave  $Z$ -rotation.

The  $Z$ -rotation is achieved as follows. Suppose the initial state of a qubit is in a superposition state  $\Psi_0 = a|0\rangle + b|1\rangle$ . After the qubit undergoes a cyclic evolution, the state  $|0\rangle$  ( $|1\rangle$ ) acquires a phase  $\xi$  ( $-\xi$ ), i.e., the state is driven to  $\Psi = a|0\rangle + be^{i\phi}|1\rangle$  with  $\phi = 2\xi$ . For a  $2\pi$  pulse ( $n = 1$ ), the induced phase  $\phi$  is given by

$$\phi = 4 \arctan(\rho/\Delta), \quad (3)$$

where the detuning is  $\Delta = \omega_D - \omega_{10}$  and  $\omega_{10}$  is the frequency difference between the lowest two transmon levels. By fixing the peak drive amplitude  $\Omega_0$  and the bandwidth  $\rho$ , we can construct a single-control  $Z$ -gate,  $Z_{\operatorname{sech}}(\Delta)$ , by adjusting only  $\Delta$ .

The specific device used for the experimental test of this gate is a concentric transmon [23, 24]. A transmon is essentially a nonlinear electrical LC oscillator that is read out using capacitive coupling, in the dispersive regime, to a linear resonator. The particular qubit used for this work had a transition frequency of  $\omega_{10} = 2\pi \times 5.18$  GHz and an anharmonicity of  $\omega_{10} - \omega_{21} = 2\pi \times 200$  MHz where  $\omega_{21}$  is the transition frequency between the first and second excited states of the transmon. Further details of the qubit and the heterodyne readout method are given in appendices A and B.

In order to demonstrate the uniqueness of the sech-drive, Rabi oscillations were driven with sech-, Gaussian- and square-pulse envelopes as shown in Fig. 1. The synthesized microwave drive is generated using modulation signals from an arbitrary pulse sequencer to IQ-modulate a local oscillator. The full length of the pulse extends over  $\pm 4\sigma$ , where  $\sigma$  is the standard deviation and can be related to the bandwidth  $\rho$  by  $\sigma = \pi/(2\rho)$  for the sech-pulse. This range fully utilizes the full digitization range of the arbitrary pulse sequencer, thereby minimizing sharp cutoffs of sech- and Gaussian-envelopes. As seen in the inset of Fig. 1, the sech-pulse is slightly broader with a longer tail than the Gaussian. While improvements to the pulse shape could be made by either creating a hard on/off transition [25] or reducing leakage with derivative removal via adiabatic gate (DRAG) [22, 26, 27], in this work we have chosen to use a simple

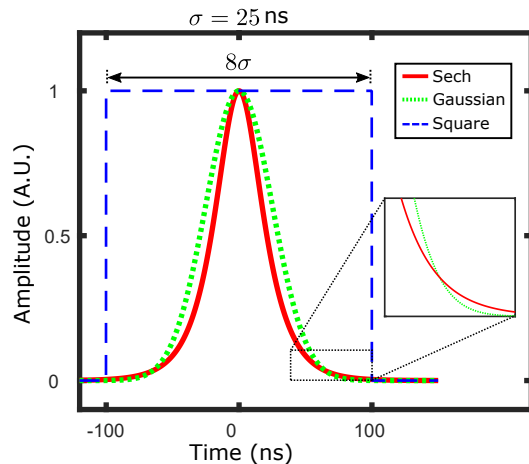


FIG. 1. (color online) Three different excitation profiles for sech-(solid red), Gaussian-(dotted green), and square-(dashed blue) pulse shapes. The sech- and Gaussian- pulses shown here are truncated at  $t = \pm 4\sigma$ , where  $\sigma$  is the standard deviation of the pulse. For the sech-pulse, the standard deviation  $\sigma$  is related to its bandwidth  $\rho$  by  $\sigma = \pi/(2\rho)$ .

sech-pulse shape for direct comparison to the theory and general purpose applications.

A comparison of experimental and theoretical Rabi oscillations versus the detuning  $\Delta$  and the pulse amplitude is shown in Fig. 2 for  $\sigma = 25$  ns pulses. The theory is simulated using the empirical result that our qubit is typically initialized in an incoherently mixed state of 90 %  $|0\rangle$  and 10 %  $|1\rangle$  due to heating in the dilution refrigerator. This results in a corresponding drop of the maximum excited-state probability. The excited-state ellipses obtained from the sech pulses are qualitatively and quantitatively different compared to the chevron-shaped response exhibited by the Gaussian and square pulses. The first feature to note is that the widths of the maxima, in the detuning axis, for the sech pulse are approximately the same for subsequent oscillation maxima [Fig. 2(a)]. If we take cuts of the images along constant detunings, this leads to uniform periodic oscillations in the excited-state probability as a function of pulse amplitude in the case of the sech, as shown in the 1-D plots of Fig. 3(a). On the other hand, the Gaussian maxima in Fig. 2(b) progressively widen and curve further downward with each oscillation period. The 1-D slices shown in Fig. 3(b) for the Gaussian illustrate that the points where the population returns to the ground state shift toward lower pulse amplitude, while the Rabi oscillation contrast grows with increasing drive strength. This behavior is further exaggerated for the square pulses, as is evident in Fig. 2(c) and Fig. 3(c). The uniformity of the oscillations in the sech-pulse case is a direct reflection of the fact that, even if the drive amplitude is fixed, one can still achieve the cyclic evolution condition. To see this effect quantitatively, the pulse amplitude required for a full Rabi cycle versus the drive detuning is plotted in Fig. 4 for all three pulse shapes. The population return

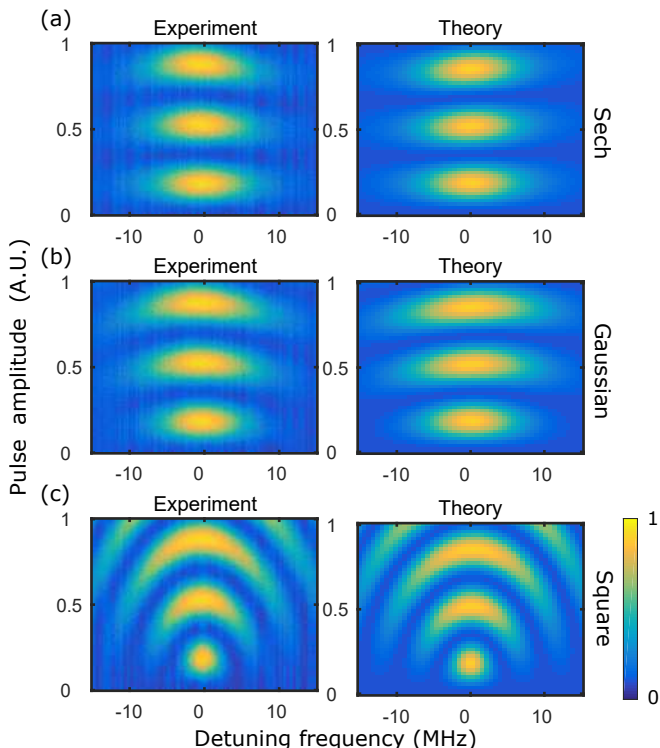


FIG. 2. (color online) The excited-state probability as a function of pulse amplitude (vertical axis) and detuning (horizontal) for (a) sech, (b) Gaussian, and (c) square pulses. The left and right panels compare experimental and theoretical simulations. The simulations include the four lowest energy levels of the transmon and decoherence process  $T_1 = T_2 = 10 \mu\text{s}$ .

amplitudes are found by quadratic fits near the minimum region which corresponds to  $2\pi$  pulses in Fig. 2. The sech-pulse only has a 8.2 % variation in the pulse amplitude over the  $|\Delta| \leq 10$  MHz range, while the Gaussian-pulse has a 43.5 % change. This low detuning-dependence behavior allows us to vary only one parameter, the detuning  $\Delta$ , to obtain an arbitrary  $Z$ -gate.

Although the experimental and theoretical results in Fig. 2(a) are in very good agreement, we do expect non-ideality in the sech data from two sources. First, the finite bit resolution cutoff at  $\pm 4\sigma$  results in a slight flattening of the third Rabi excitation ellipse in the experimental plot of Fig. 2(a). The second possible source is the existence of higher levels of the transmon system, resulting in a slight tilt of the theoretical Rabi ellipses. This behavior is illustrated in the simulation for multiple Rabi oscillations. This effect is most likely masked in the experiment by the finite bit resolution of the arbitrary pulse sequencer. However, note that only the first oscillation (about 1/3 of the  $Y$ -axis range in Fig. 2(a)) is used to implement  $Z$ -gates, and for this region there is negligible discrepancy between theory and experiment. This high degree of frequency independence explains the very high fidelities we obtained, as we discuss below.

The preparation and tomography pulse sequence for

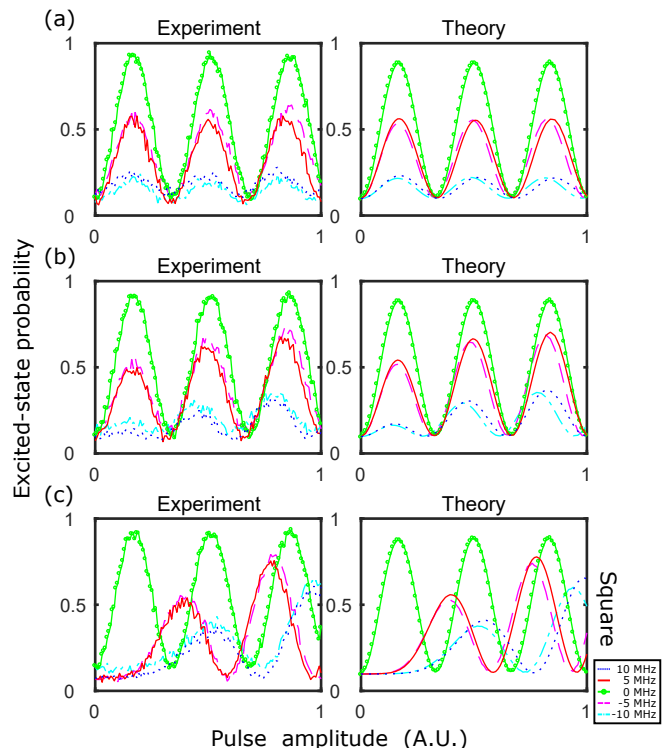


FIG. 3. (color online) Line cuts at various detunings versus pulse amplitude from Fig. 2.

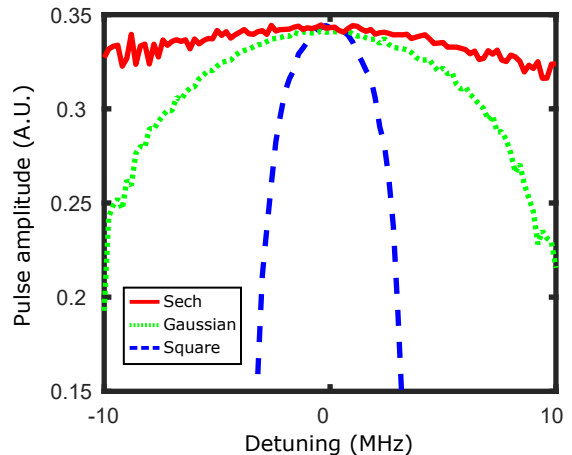


FIG. 4. (color online) The pulse amplitude for the first full Rabi cycle plotted versus the drive detuning for sech (solid red), Gaussian (dotted green), and square (dashed blue) pulse shapes.

the  $Z_{\text{sech}}(\Delta)$  phase gate is shown in Fig. 5(a). In this example, the state is initially prepared by a  $\pi/2$  rotation around the  $-Y$ -axis. A subsequent  $2\pi$ -sech-pulse is then applied with the drive frequency given by  $\omega_D = \Delta + \omega_{10}$ , and in each experimental run, either the  $X$ -,  $Y$ -, or  $Z$ -projection of the final state is measured to complete the single-qubit tomography. From this, the resulting  $\phi(\Delta)$  and  $\theta(\Delta)$  are determined, where  $\theta$  is the angle of the

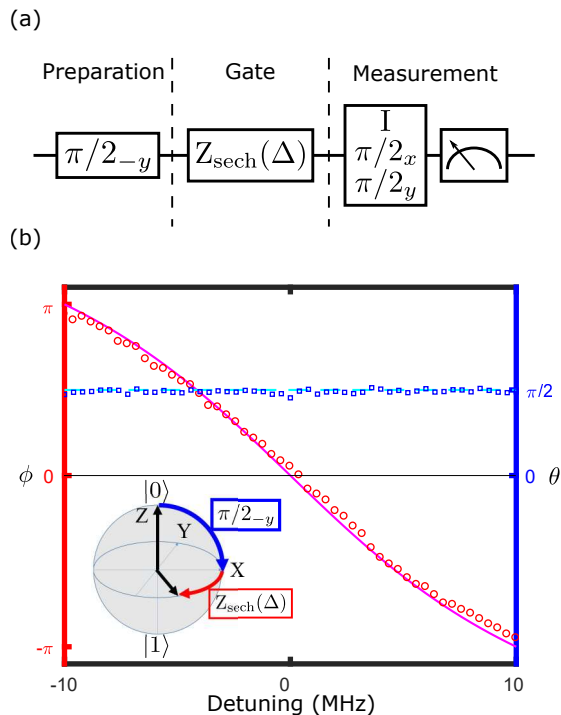


FIG. 5. (color online) Tomography of a single-qubit phase gate,  $Z_{\text{sech}}(\Delta)$ , for a state prepared by a  $\pi/2$  rotation. Panel (a) shows the pulse sequence and panel (b) shows the theory predicted  $\theta$  (dashed cyan line) and  $\phi$  (solid magenta line) and the measured  $\theta$  (blue square) and  $\phi$  (red circle), where  $\theta$  and  $\phi$  are the polar and azimuthal angles of the resulting Bloch vector of the qubit state.

Bloch vector from the  $Z$ -axis [solid points in Fig. 5(b)]. For  $-10 \text{ MHz} \leq \Delta \leq 10 \text{ MHz}$ , these data show that  $\theta$  remains constant at  $\pi/2$ . This demonstrates that the rotation of the Bloch vector is around the  $Z$ -axis with rotation angle  $\phi$ . Both are in excellent agreement with the prediction, Eq. (3) [the solid lines in Fig. 5(b)].

To assess the performance of our  $Z_{\text{sech}}(\Delta)$  gate, we consider the fidelity of the rotations for the six input states obtained from  $\pi/2$  rotations about the  $\pm X$ ,  $\pm Y$  directions, the identity operator, and a  $\pi$  rotation. To account for the existence of mixed states in the initial state preparation, we calculate the fidelity of the gate operation,  $Z_{\text{sech}}(\Delta)$  as

$$F = \text{Tr} \left[ \sqrt{\sqrt{\rho_1} \rho_2 \sqrt{\rho_1}} \right], \quad (4)$$

for each of the initial states. The density matrix  $\rho_1$  is reconstructed from tomography measurements and  $\rho_2$  is calculated from the theory, Eq. (3), with a 9 % excited state before the state preparation pulse. Complete tomography results for all six possible initial states are presented in appendix C. As shown in Fig. 6, the fidelity averaged over the six different initial states is  $F_{\text{avg}}(\Delta) > 99 \%$  for  $|\Delta| \leq 10 \text{ MHz}$ . This range corresponds to a  $\mp\pi$  rotation around the  $Z$ -axis. For  $|\Delta| \geq 10 \text{ MHz}$ , there is

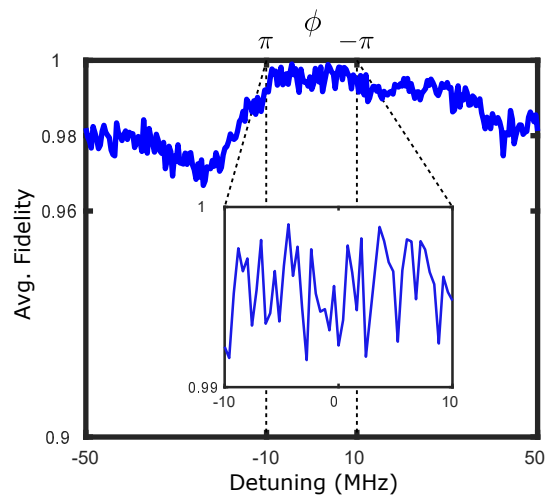


FIG. 6. (color online) The average fidelity for the sequence in Fig. 5(a) averaged over the six different initial states prepared as described in the text.

a slight drop-off of  $F_{\text{avg}}$  for the negative detuning, presumably due to the existence of higher energy level transitions at lower frequencies due to the anharmonicity of the transmon.

In conclusion, we have shown that an ideal sech-shaped pulses can be used to implement a fast, high-fidelity phase gate with a single control knob, the detuning. The unique properties of the sech drive allow us to achieve this gate while staying in the computational subspace throughout the duration of the gate. Our work paves the way toward high-fidelity two- and three-qubit entangling phase gates, which have been theoretically proposed based on the sech pulse [15, 16]. Moreover, the sech drive can be advantageous when the lowest energy levels have some spread, as is intrinsic to the superconducting devices manufactured with lithographically defined and thermally oxidized components. Our results also lay the ground work for the superconducting circuit-based experimental demonstration of Self Induced Transparency [10], which occurs when, in addition to the temporal profile, the spatial distribution of the pulse is also a sech function. Such an experiment would be relevant for microwave-based logic with these circuits, slow-light demonstrations, and the development of larger scale circuits.

## ACKNOWLEDGMENTS

The authors acknowledge support of the NIST Quantum Based Metrology Initiative. This work is property of the US Government and not subject to copyright.

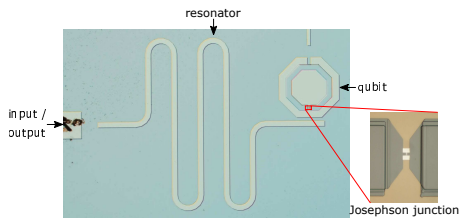


FIG. 7. (color online) Optical microscope image of the device.

### Appendix A: Device characterization

The image of the device is shown in Fig. 7. It consists of a concentric transmon [24] coupled to a microstrip resonator. The bare resonator frequency is  $\omega_r = 2\pi \times 8.5745$  GHz with a coupling  $Q_c = 5,000$  to the transmission line. The resonator-qubit coupling strength is  $g = 2\pi \times 71.4$  MHz which results in a 1.5 MHz resonator frequency shift when probed in the dispersive regime (Fig. 8). The transmon frequency is measured as  $\omega_{10} = 5.18$  GHz with an anharmonicity of  $\alpha = 200$  MHz (Fig. 9) [28]. The device is cooled down in a dilution refrigerator to a base temperature of  $T = 25$  mK. The qubit relaxation  $T_1$  and decoherence  $T_2^*$  are measured to be  $8.6 \mu\text{s}$  (Fig. 10) and  $10.25 \mu\text{s}$  (Fig. 11), respectively.

### Appendix B: Qubit control and measurement system

The synthesized microwave drive is generated by IQ-modulating a local oscillator (LO) as shown in Fig. 12(a). The two modulation signals, I and Q, are produced from an arbitrary pulse sequencer with pre-programmed pulse shapes such as sech, Gaussian or square functions. The amplitude ratio between I and Q allows for an arbitrary phase of the output pulse relative to the LO, which defines the rotation axis. The pulse amplitudes are calibrated to  $\pi/2$  and  $\pi$  rotations by applying repeated pulses to amplify small errors [29]. DC offsets are added in I and Q signals to suppress LO leakage. The IQ modulator is followed by a variable attenuator and a fast microwave switch for an additional power control and better on/off ratio.

Our two-channel heterodyne microwave measurement system is shown in Fig. 12(b) [30]. This scheme is typically referred to as interferometric readout. Each of the measurement channel uses two microwave synthesizers, a LO and a Readout, with a frequency difference  $\omega_{\text{IF}}$  between them. The two generator are both split into two paths. In one path, the LO and the Readout are directly mixed down to generate a reference tone. In the other path the Readout is passed through the device under test and then mixed with the LO to generate the signal encoded with the qubit state information. The signal and the reference are both digitized in the computer. The amplitude and phase of the signal relative to the reference are then extracted in the control program.

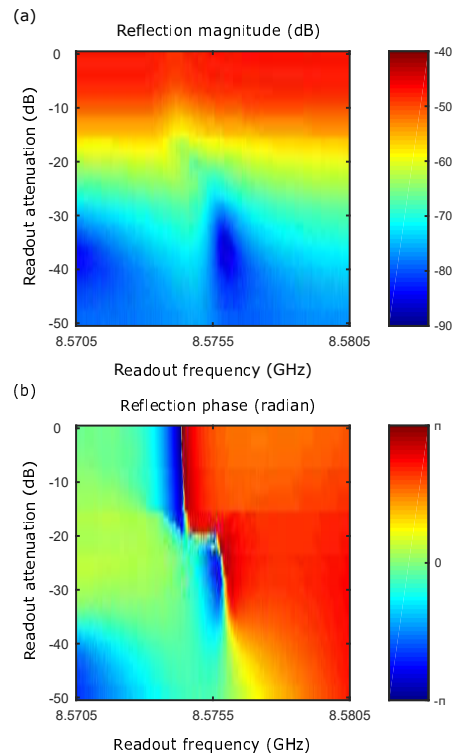


FIG. 8. (color online) Color scale of readout resonator response [(a) magnitude (b) phase] vs. frequency (x-axis) and power (y-axis).

The advantage of the interferometric readout is that it is not necessary to calibrate an IQ mixer vs. frequency for single-sideband modulation. This comes at the cost of an extra synthesizer in the setup, but makes searching for readouts much easier.

### Appendix C: Single-qubit tomography

Tomographies for our  $Z_{\text{sech}}(\Delta)$  gate operating on six different initial states (sequence illustrated in Fig. 5(a) of main text) are shown in Fig. 13. The measurements (solid points) and theory (solid lines) agree with each other well for  $|\Delta| \leq 10$  MHz, which correspond to a full  $2\pi$  rotation around the  $Z$ -axis. For  $|\Delta| \geq 10$  MHz, the increased deviations between them are due to the pulse cutoff at  $\pm 4\sigma$  and the existence of higher levels of the transmon qubit.

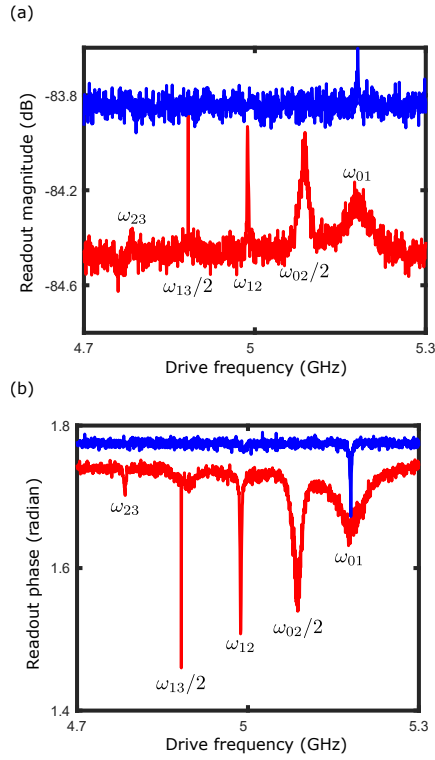


FIG. 9. (color online) Readout resonator response [(a) magnitude (b) phase] vs. qubit drive frequency showing the qubit energy spectra for high (red/lower line) and low (blue/upper line) driver powers.

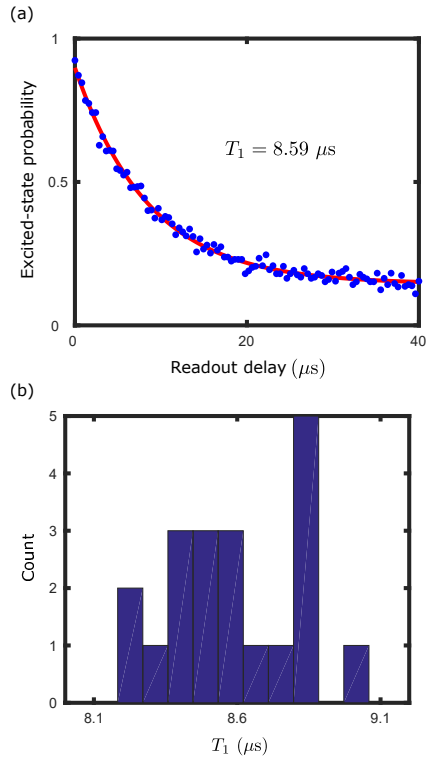


FIG. 10. (color online) (a) Energy decay,  $T_1$  of qubit (b) Histogram of multiple  $T_1$  measurements over one hour.

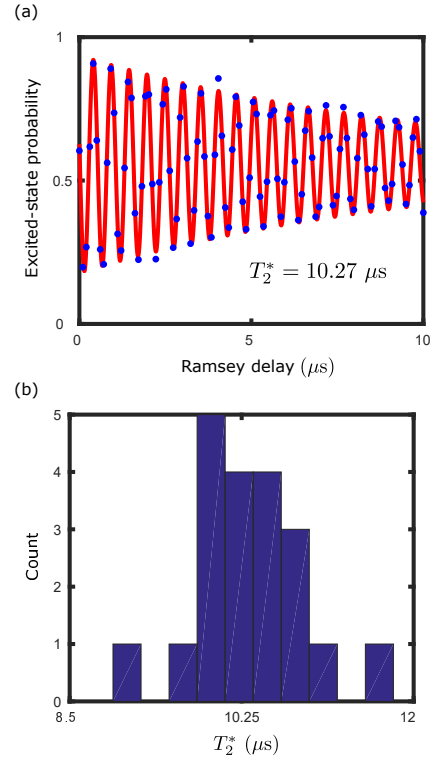


FIG. 11. (color online) (a) Phase decoherence,  $T_2^*$  of qubit (b) Histogram of multiple  $T_2^*$  measurements over one hour.

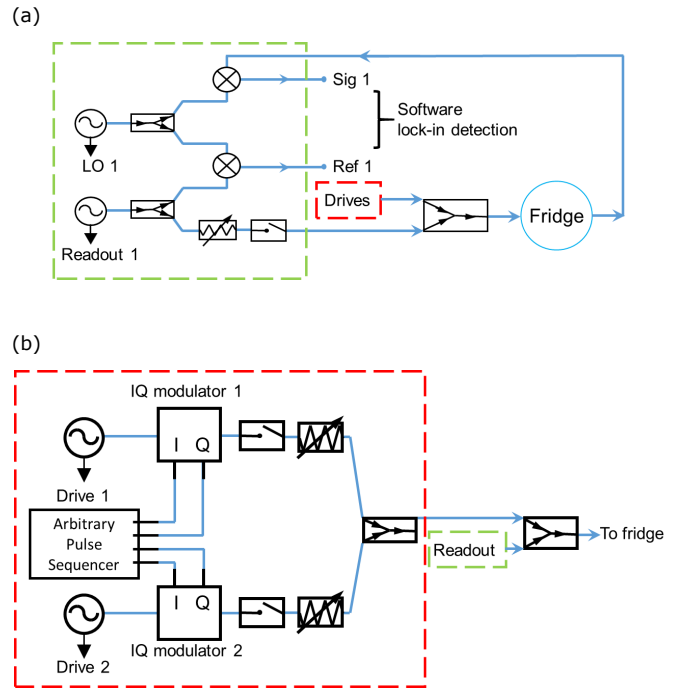


FIG. 12. (color online) (a) Schematic for the generation of the pulse-shaped microwave drive. Drive 1 is the  $Z_{\text{sech}}(\Delta)$  gate and drive 2 is for the state preparation and tomography rotations. (b) Schematic for the generation of the pulse-shaped microwave drive. Drive 1 is the  $Z_{\text{sech}}(\Delta)$  gate and drive 2 is for the state preparation and tomography rotations.

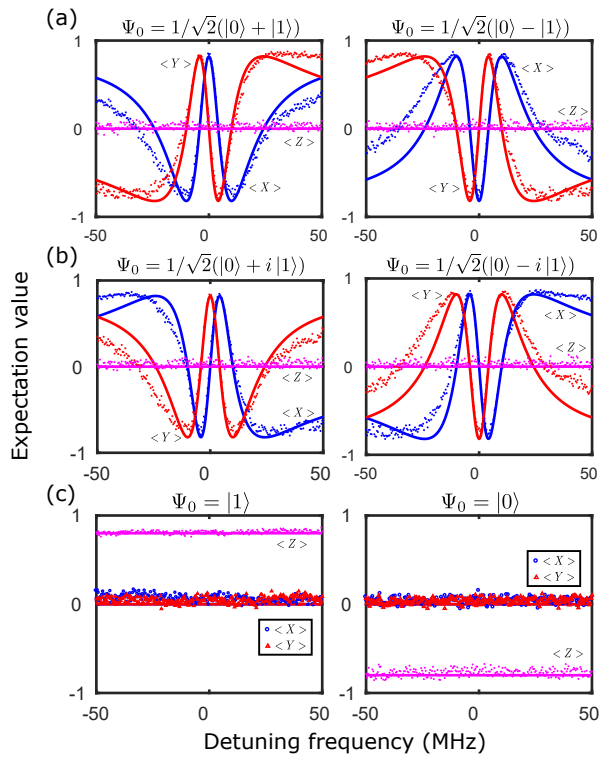


FIG. 13. (color online) Tomographies of the  $Z_{\text{sech}}(\Delta)$  gate for states initially prepared by a (a)  $Y_{-\pi/2}$ , (b)  $Y_{\pi/2}$ , (c)  $X_{\pi/2}$ , (d)  $X_{-\pi/2}$ , (e)  $X_{\pi}$ , (f)  $I$  rotation.

- 
- [1] T. D. Ladd, F. Jelezko, R. Laflamme, Y. Nakamura, C. Monroe, and J. L. O'Brien, *Nature* **464**, 45 (2010).
- [2] N. Gisin, G. Ribordy, W. Tittel, and H. Zbinden, *Rev. Mod. Phys.* **74**, 145 (2002).
- [3] C. L. Degen, F. Reinhard, and P. Cappellaro, *ArXiv e-prints* (2016), 1611.02427.
- [4] M. H. Devoret and R. J. Schoelkopf, *Science* **339**, 1169 (2013).
- [5] T. E. Phipps and O. Stern, *Zeits. f. Physik* **73**, 185 (1932).
- [6] C. C. Gerry and P. L. Knight, *Introductory Quantum Optics* (Cambridge University Press, Cambridge, UK, 2005), ISBN 0 521 82035, section 4.4.
- [7] N. Rosen and C. Zener, *Phys. Rev.* **40**, 502 (1932).
- [8] G. Lamb, *Rev. Mod. Phys.* **43**, 99 (1971).
- [9] M. Segev, B. Crosignani, A. Yariv, and B. Fischer, *Phys. Rev. Lett.* **68**, 923 (1992).
- [10] S. L. McCall and E. L. Hahn, *Phys. Rev.* **183**, 457 (1969).
- [11] J. M. S. Lehto and K.-A. Suominen, *Phys. Scr.* **91**, 013005 (2016).
- [12] S. E. Economou, L. J. Sham, Y. Wu, and D. G. Steel, *Phys. Rev. B* **74**, 205415 (2006).
- [13] S. E. Economou and T. L. Reinecke, *Phys. Rev. Lett.* **99**, 217401 (2007).
- [14] S. E. Economou, *Phys. Rev. B* **85**, 241401 (2012).
- [15] S. E. Economou and E. Barnes, *Phys. Rev. B* **91**, 161405 (2015).
- [16] E. Barnes, C. Arenz, A. Pitchford, and S. E. Economou, *ArXiv e-prints* (2016), 1612.09384.
- [17] R. Barends, J. Kelly, A. Megrant, A. Veitia, D. Sank, E. Jeffrey, T. C. White, J. Mutus, A. G. Fowler, B. Campbell, et al., *Nature* **508**, 500 (2014).
- [18] B. R. Johnson, M. P. da Silva, C. A. Ryan, S. Kimmel, J. M. Chow, and T. A. Ohki, *New J. Phys.* **17**, 113019 (2015).
- [19] J. Z. Blumoff, K. Chou, C. Shen, M. Reagor, C. Axline, R. T. Brierley, M. P. Silveri, C. Wang, B. Vlastakis, S. E. Nigg, et al., *Phys. Rev. X* **6**, 031041 (2016).
- [20] M. A. Rol, C. C. Bultink, T. E. O'Brien, S. R. de Jong, L. S. Theis, X. Fu, F. Luthi, R. F. L. Vermeulen, J. C. de Sterke, A. Bruno, et al., *ArXiv e-prints* (2016), 1611.04815.
- [21] M. Steffen, M. Ansmann, B. Radoslaw, N. Katz, E. Lucero, R. McDermott, M. Neeley, E. Weig, A. Cleland, and J. Martinis, *Science* **313**, 1423 (2006).
- [22] D. C. McKay, C. J. Wood, S. Sheldon, J. M. Chow, and J. M. Gambetta, *ArXiv e-prints* (2016), 1612.00858.
- [23] M. Sandberg, M. R. Vissers, T. A. Ohki, J. Gao, J. Aumentado, M. Weides, and D. P. Pappas, *Appl. Phys. Lett.* **102**, 072601 (2013).
- [24] J. Braumuller, M. Sandberg, M. R. Vissers, A. Schneider, S. Schlr, L. Grnhaupt, H. Rotzinger, M. Marthaler, A. Lukashenko, A. Dieter, et al., *Appl. Phys. Lett.* **108**, 032601 (2016).
- [25] J. M. Martinis and M. R. Geller, *Phys. Rev. A* **90**, 022307 (2014).
- [26] F. Motzoi, J. M. Gambetta, P. Rebentrost, and F. K. Wilhelm, *Phys. Rev. Lett.* **103**, 110501 (2009).
- [27] T. Kaufmann, T. J. Keller, J. M. Franck, R. P. Barnes, S. J. Glaser, J. M. Martinis, and S. Han, *J. Magn. Reson.* **235**, 95 (2013).
- [28] J. Koch, T. M. Yu, J. Gambetta, A. A. Houck, D. I. Schuster, J. Majer, A. Blais, M. H. Devoret, S. M. Girvin, and R. J. Schoelkopf, *Phys. Rev. A* **76**, 042319 (2007), URL <http://link.aps.org/doi/10.1103/PhysRevA.76.042319>.
- [29] J. M. Chow, Ph.D. thesis, Yale University (2010).
- [30] K. L. Geerlings, Ph.D. thesis, Yale University (2013).